RSC Advances

PAPER



Cite this: *RSC Adv.*, 2021, **11**, 30503

# Facile synthesis of nitrogen-defective g-$C_3N_4$ for superior photocatalytic degradation of rhodamine B†

Xiupei Yang, *[a] Lin Zhang,[a] Dan Wang,[a] Qian Zhang,[a] Jie Zeng[a] and Run Zhang *[b]

Developing a new photocatalyst for fast and highly efficient organic dye degradation plays an essential role in wastewater treatment. In this study, a photocatalyst graphite phase carbon nitride (g-$C_3N_4$) containing nitrogen defects (CN) is reported for the degradation of rhodamine B (RhB). The porous g-$C_3N_4$ photocatalyst is facilely synthesized through a polycondensation method and then characterized by X-ray diffraction (XRD), infrared spectroscopy (FT-IR), field emission scanning electron microscopy (FESEM), $N_2$ isotherm adsorption line, and X-ray photoelectron spectroscopy (XPS). The photocatalytic activity of the g-$C_3N_4$ is evaluated through the degradation of RhB under visible light irradiation. The results show that photocatalytic activity of the nitrogen-defective g-$C_3N_4$ can be improved by optimizating washing conditions, including washing temperature, washing dosage, drying time, and drying temperature. With the prepared nitrogen-defective g-$C_3N_4$, decolourization of RhB is able to be completed within 20 minutes, in which the degradation rate is 1.7 times higher than that of bulk g-$C_3N_4$. Moreover, the nitrogen-defective g-$C_3N_4$ has high stability and reusability in the degradation of RhB. Photocatalytic degradation mechanism investigations by ultraviolet-visible absorption spectroscopy, radical trapping experiments and high-performance liquid chromatography (HPLC) reveal that RhB achieved complete mineralization through the photocatalytic degradation reaction mediated by superoxide radicals ($^{\bullet}O_2^-$). This work thus provides a new approach for the preparation of photocatalysts for organic pollutants treatment in wastewater samples.

Received 19th July 2021
Accepted 7th September 2021

DOI: 10.1039/d1ra05535f

rsc.li/rsc-advances

## Introduction

In recent years, the rapid growth of industry has led to the excessive use of chemical raw materials.[1] The precautions of the negative impacts of this situation were inadequate, which has led to a global crisis, including resource shortages, pollution of the living environment (water pollution, air pollution, and soil pollution), and ecological pollution damage. Among them, environmental pollution has become a prominent problem faced by humankind;[2] the quality of water changes and air pollution seriously affect human health and development.[3] Of the environmental pollutions, water pollution is one of the most serious issues and worthy of concern.[4,5] As a basic dye, RhB has been widely used in food processing as an additive until the discovery of its carcinogenicity in recent years. Although this organic dye has been banned from being used in food industries, RhB remains widely used in papermaking, textile printing and dyeing, leather manufacturing, coloured glass colouring, cell fluorescence staining, dyeing, and fireworks manufacturing industries.[6,7] Wastewater from these industries generally contains high concentrations of RhB and other organic dyes that cause a series of environmental pollution problems.[8,9] Therefore, an efficient and economical method is highly demanded to treat the organic dye (particularly RhB) contamination in wastewater.

Photocatalytic technology is a green, efficient, and extremely low-energy method that can convert light into chemical energy for wastewater purification.[10,11] This technology is able to solve the problems of energy shortage and environmental pollution,[12] thus has been received extensive attention in recent years in the field of organic dyes degradation. In this context, semiconductor photocatalysts, such as titanium dioxide ($TiO_2$), zinc oxide (ZnO), and graphite carbon nitride (g-$C_3N_4$),[13,14] have been developed as the catalyst materials for photochemical reactions under the action of light. These materials are featured with excellent photoelectric properties and suitable energy band structure, which can convert abundant solar energy, a natural energy source, into valuable chemical resources for photochemical reactions. Of these photocatalysts, g-$C_3N_4$ has a similar 2D layered structure to graphene,[15] in which the plane layers are connected by the basic structural unit's C–N bond-the

[a]College of Chemistry and Chemical Engineering, Chemical Synthesis and Pollution Control Key Laboratory of Sichuan Province, China West Normal University, Nanchong 637000, China. E-mail: xiupeiyang@163.com

[b]Australian Institute for Bioengineering and Nanotechnology, The University of Queensland, Brisbane, Queensland 4072, Australia. E-mail: r.zhang@uq.edu.au

† Electronic supplementary information (ESI) available. See DOI: 10.1039/d1ra05535f

tri-*s*-triazine pyrimidine unit (heptazine ring), and the layers are connected by week van der Waals forces.[16] Due to its merits of earth abundance, environmental friendliness, chemical stability, and proper band position in the redox reaction of water, g-$C_3N_4$ has attracted great attention in the field of photocatalysis.[17] However, bulk g-$C_3N_4$ has low photocatalytic efficiency as its low specific surface area, limited light absorption, and easy recombination of photo-generated carriers.[16,18] Following research found that the photocatalytic activity can be improved through modifying g-$C_3N_4$'s morphology,[19–21] element doping,[22–24] and semiconductor compounding,[25–27] advancing the applications of g-$C_3N_4$ in photocatalysis.[28,29] In these modification methods, the morphology control is a simple and effective way to adjust the surface structure to improve photocatalytic activity without introducing additional unit components during the synthesis process of the modified g-$C_3N_4$.[30]

In this work, a porous g-$C_3N_4$ photocatalyst with nitrogen defects was developed for the photodegradation of RhB organic dyes (Scheme 1). The photocatalyst was synthesized by a simple precursor treatment combined with a one-step calcination method. The photocatalyst was then characterized by X-ray diffraction (XRD), infrared spectroscopy (FT-IR), scanning electron microscopy (SEM), $N_2$ adsorption isotherm, and X-ray photoelectron spectroscopy (XPS), and then was used to simulate visible light catalytic degradation of RhB dye wastewater. By optimizing the four washing conditions of precursor, including washing temperature, washing dosage, drying time, and drying temperature, the optimal conditions for washing modification were discussed. In comparison with the unmodified bulk g-$C_3N_4$, the prepared nitrogen-deficient porous g-$C_3N_4$ exhibits stronger photocatalytic performance for RhB degradation.

# Experimental

## Materials

The precursor melamine and the dye rhodamine B were obtained from Aladdin Industrial Corp. (Shanghai, China). Methylene blue (MB) and methyl orange (MO) came from domestic commercial suppliers. All chemicals were analytical reagent grade and used without further purification. The ultrapure water used in the experiment was made by the laboratory.

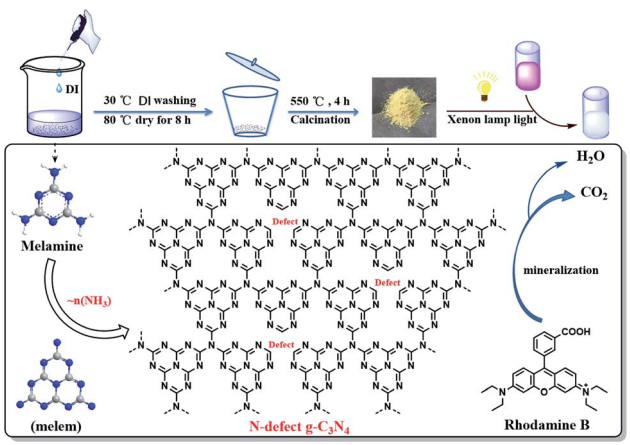


Scheme 1 Schematic illustration the design and the synthesis of nitrogen-deficient porous g-$C_3N_4$ photocatalyst for photocatalytic degradation of RhB.

## Preparation of nitrogen-defective g-$C_3N_4$

Nitrogen-defective g-$C_3N_4$ was synthesized using a facile polycondensation method. First, 2.0 g of melamine was added into 10 mL of deionized water, heated and stirred in a water bath at 30 °C for 10 min, and then dry at 80 °C for 8 h. Then, the product was grinded evenly with an agate mortar to obtain a powdery modified precursor. The calcination condition of precursor refers to the preparation of bulk g-$C_3N_4$.[31] In addition, the water treated precursor was transferred into a muffle furnace and heat to 550 °C and hold for 4 h at a heating rate of 2 °C $min^{-1}$. After the natural cooling to room temperature, taken out and grinded uniformly again, the yellow powder obtained is the target product, nitrogen-defective g-$C_3N_4$ (CN). As a control, 2.0 g of melamine was directly calcined under the same muffle furnace calcination conditions to obtain the bulk g-$C_3N_4$ (BCN).

## Characterization of nitrogen-defective g-$C_3N_4$

Morphology of catalyst materials of the scanning electron microscope (SEM) was obtained from Carl Zeiss, Gemini 500 (Carl Zelss, Shanghai). The crystal structure of the photocatalyst was determined by X-ray diffractometry (XRD, Rigaku Dmax/Ultima IV). The recombination rate of photogenerated electrons and holes of the photocatalyst were determined by a fluorescence spectrometer (PL, Hitachi F-4600) at room temperature. X-ray photoelectron spectra (XPS) were taken on a ThermoFischer, ESCALAB Xi+ (Thermo Fisher Scientific, USA). Fourier transform infrared spectra (FTIR) were recorded with a Nicolet 6700 spectrometer (Thermo Electron Corporation, USA). All ultraviolet-visible (UV-vis) absorption spectra were conducted with a Shimadzu UV-2550 UV-vis absorption spectrophotometer (Kyoto, Japan). UV-visible diffuse reflectance spectroscopy (DRS, Shimadzu UV-3600) was used to analyse the light absorption performance of the photocatalyst, and $BaSO_4$ was used as the reference standard. The specific surface area and pore size distribution of the photocatalyst were characterized using an ASAP 2020 (USA).

## Optimization of synthesis conditions

The experiment used the controlled variable method to discuss and optimize the precursor washing conditions, including washing temperature, dosage, drying temperature, and time.

## Photocatalytic degradation experiment

Under simulated visible light irradiation, the photocatalytic activity of the product catalyst was compared by comparing the photodegradation efficiency of RhB to find the better water washing modification conditions. The specific experimental steps were as follows, taking 50 mg of catalyst sample and dispersing uniformly in 50 mL of RhB solution (10 mg $L^{-1}$), and stirring for 1 hour in the dark to ensure that the photocatalyst and RhB molecules reach an adsorption–desorption

equilibrium state. In the experiment, a 300 W xenon lamp (with a 420 nm cut-off filter) was used as a visible light source to illuminate the suspension. During the irradiation about 3 mL of the suspension was sampled at the interval of every 5 minutes and then centrifuged to remove the photocatalyst powder. The absorbance of RhB at 554 nm at each time point was measured using a UV-2550 ultraviolet-visible spectrophotometer. According to Lambert Beer's law eqn (1), the absorbance ($A$) is proportional to the solution concentration ($C$), so the solution degradation rate ($\eta$) at $t$ min can be calculated by the following formula:

$$A = KLC \quad (1)$$

$$\eta = (C_0 - C_t)/C_0 \times 100\% \quad (2)$$

where $A$ represents the absorbance of RhB dye solution at the maximum absorption wavelength of 554 nm, $K$ represents the molar absorbance coefficient, $L$ is the thickness of the absorption layer, $C$ is the concentration of the solution, $\eta$ represents the degradation rate of the dye solution at $t$ min.

First-order kinetic model simplified from Langmuir Hinshelwood (L–H) model is introduced to describe the photocatalysis reaction:

$$-\ln(C_t/C_0) = Kt \quad (3)$$

where $C_t$ is the concentration at $t$ min, $C_0$ is the initial concentration of RhB and $K$ represents the reaction rate constant.

### The light absorption performance and band gap $E_g$

The optical band gap of CN and BCN was calculated from the UV-vis absorption spectra based on $BaSO_4$. According to the following formula (4), the intersection point between the tangent line and the $X$-axis is the band gap width $E_g$.[31]

$$(\alpha h\nu)^{1/2} = A(h\nu - E_g) \quad (4)$$

where $\alpha$, $h$, $\nu$, $A$ represent the absorbance index, Planck's constant, frequency, and constant, respectively. The optical band gap is represented by $E_g$.

### Cycle experiment

The stability of the synthetic material CN was verified by cyclic degradation experiments. After each cycle, all the catalysts in the reaction system were recovered, washed repeatedly with deionized water and anhydrous ethanol to remove the dye molecules on the surface, dried overnight in a vacuum at 60 °C and ground evenly before being used for the next cycle.

### Research on photocatalytic mechanism

The reactive species were explored through free radical capture experiments to explain the mechanism of the photocatalytic degradation of RhB. Isopropanol (IPA), $p$-benzoquinone (BQ) and disodium ethylenediaminetetraacetic acid (EDTA-2Na) were added to three independent photodegradation systems as hydroxyl radical ($^{\bullet}OH$), superoxide radical ($^{\bullet}O_2^-$) and photogenerated hole ($h^+$) trapping agents, respectively. High-performance liquid chromatography (HPLC) was used to analyse the initial RhB solution and the degraded products to reveal the degradation pathway and mechanism.[21]

## Results and discussion

### Preparation and characterization of CN

As is shown in Scheme 1, porous g-$C_3N_4$ photocatalyst with nitrogen defect (CN) was synthesized by a simple precursor treatment and one-step calcination using melamine as the source of carbon and nitrogen. CN has good reusability and chemical stability, and can serve as a material for photocatalytic degradation of organic dyes such as RhB, MO and MB (Fig. S1†). In comparison with BCN, the porous g-$C_3N_4$ photocatalyst (CN) shows higher efficiency for RhB dye degradation under simulated visible light irradiation as evidenced by the completion of RhB decolorization within 20 minutes.

The morphologies of BCN and CN were characterized by scanning electron microscopy (SEM). As shown in Fig. 1a–d, the surface of BCN is smooth and agglomerated. A large number of pores are observed for the CN surface, indicating that more reactive sites on the CN's surface and thus higher photocatalytic efficiency are expected for CN. The EDS-mapping spectra of CN (Fig. 1e–g) show that C and N elements are evenly distributed in the photocatalytic materials of CN.

The phase structure of the catalyst was then determined by X-ray powder diffraction (XRD). Fig. 2a shows the X-ray diffraction patterns of BCN and CN. Both CN and BCN have two characteristic absorption peaks of g-$C_3N_4$,[32] indicating the successful preparation of modified g-$C_3N_4$ through the water-washed melamine precursor method. Specifically, the diffraction peak of the material at $2\theta = 13.1°$ corresponds to the (100) crystal plane of g-$C_3N_4$, which is attributed to the in-plane tri-$s$-triazine repeating structural unit.[33] The diffraction peak at $2\theta = 27.3°$ corresponds to the (002) crystal plane, which is produced by the interlayer stacking of conjugated aromatic rings of g-

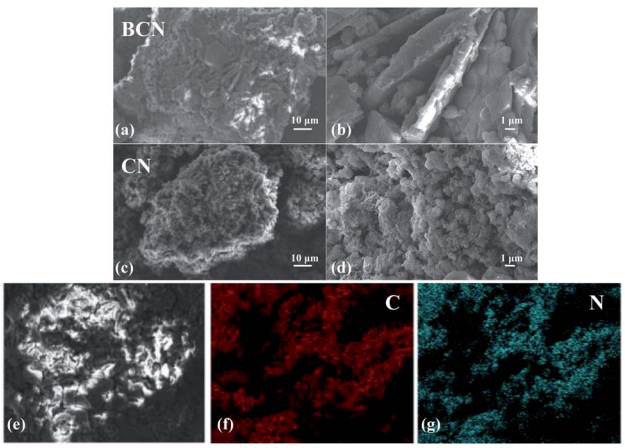


Fig. 1 SEM images of (a and b) BCN, (c and d) CN and (e–g) EDS-mapping spectra of CN.

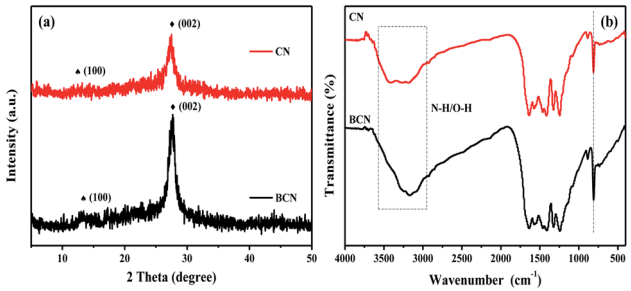


Fig. 2 (a) XRD patterns and (b) FT-IR spectra of BCN and CN.

$C_3N_4$.[34–36] In comparison with BCN, the weaker characteristic diffraction peaks of CN could be attributed to the formation of hydrogen bonds between the melamine precursor molecules and the water molecules during the washing process. In the process of washing melamine with water, water molecules were connected to melamine molecules through hydrogen bonds and electrostatic interactions, increasing the distance between melamine molecules. The hydrogen bond interaction was weakened during the thermal polymerization process, which reduced the degree of polymerization during the calcination process.[37–39] The bridging N atom and the terminal amino group of the melamine molecule were relatively reduced, and the connection of the formed tri-*s*-triazine structural units was reduced. As a result, the layer structure units in g-$C_3N_4$ were reduced, and the interlayer stacking force was weakened, which was conducive to the formation of defect g-$C_3N_4$. Moreover, as shown in Fig. S2,† similar XRD patterns were obtained for the g-$C_3N_4$ synthesized under different washing conditions, including water treatment temperature and time, and drying temperature and time, indicating that the proposed g-$C_3N_4$ photocatalysts can be easily synthesized by precursor treatment combined with one-step calcination method.

The structure of the product was also confirmed by the infrared spectrum. As shown in Fig. 2b, the broad peak at about 3000–3800 $cm^{-1}$ corresponds to the stretching vibration of the intermolecular N–H bond and O–H bond. The multiple absorption peaks at 1200–1700 $cm^{-1}$ are attributable to the stretching vibrations of N=C and N–$(C)_3$ in the CN heterocyclic ring,[40] and the sharp peak at 813 $cm^{-1}$ is the characteristic absorption of g-$C_3N_4$, which is the characteristic respiratory vibration of the triazine structural unit.[41] The absorption peaks of the material are in good agreement with those of the original bulk g-$C_3N_4$. As showing in Fig. S3,† similar FTIR spectra were also obtained for the g-$C_3N_4$ synthesized under different washing conditions, indicating the successful synthesis of the g-$C_3N_4$ photocatalyst. Comparing the broad peaks around 3000–3800 $cm^{-1}$ and the sharp peaks at 813 $cm^{-1}$ between BCN and CN, the absorption of CN was significantly weakened, and the intensity of multiple absorption peaks at 1200–1700 $cm^{-1}$ was also weakened to a certain extent. This might be due to the existence of nitrogen defects, which destroyed the structural integrity of tri-*s*-triazine structural units.[42] It further showed that the degree of polymerization of CN was lower than that of BCN, which was consistent with the above-mentioned XRD analysis results.

XPS spectra of the BCN and CN photocatalysts were then recorded for further investigating the surface composition and chemical structure. As shown in Fig. 3a, the XPS full spectrum shows that both BCN and CN have C, N, and O elements. The C and N elements came from the photocatalytic material itself, and O mainly came from $H_2O$ and $O_2$ molecules absorbed on the photocatalyst. The C 1s high-resolution spectra of both BCN and CN show characteristic peaks at 288.3 and 284.9 eV (Fig. 3b and c), corresponding to the $sp^2$-hybridized C (N=C–N) in the aromatic ring and the $sp^2$ C–C bonds in adventitious carbon species.[43] The N 1s spectra of both BCN and CN exhibit four characteristic peaks (Fig. 3d–e). The highest binding energy at 398.6 eV is attributable to C=N–C in the triazine ring, and the binding energies at 399.4 eV and 401.2 eV are attributed to the $sp^2$ hybrid N in N–$(C)_3$ and the amino functional group N–H, respectively. The weaker peak at 404.6 eV could be attributed to the charge effects or charge localization effects.[44,45]

The chemical composition of CN was also analysed by N 1s peak fitting, and the data were presented in Table 1. The $sp^2$ hybrid N in N–$(C)_3$ and the terminal amino functional group N–H in CN are significantly lower than those of BCN. According to the distribution of N 1s binding energy, it could be seen that the N defects in CN were mainly caused by the loss of bridging $sp^2$ N atoms and terminal amino groups. Table S1† of the EDS elemental analysis results showed that the C/N molar ratios in

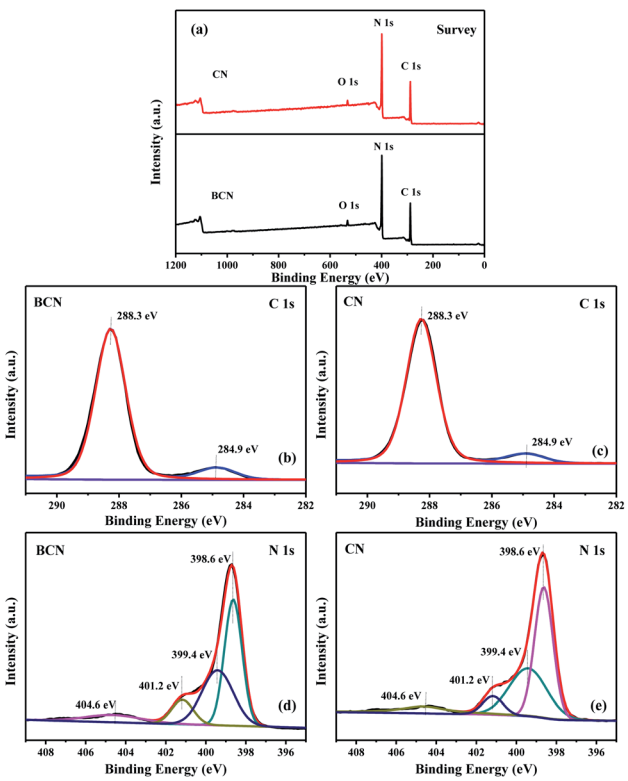


Fig. 3 (a) XPS full spectrum, (b and c) C 1s high-resolution spectrum, (d and e) N 1s high-resolution spectrum of BCN and CN.

Table 1 Covalent bond distribution of N 1s binding energy of BCN and CN

| Binding energy | 398.6 eV (C=N–C) | 399.4 eV (N–$(C)_3$) | 401.2 eV (C–N–H) | 404.6 eV (charge effects) |
|---|---|---|---|---|
| BCN | 45.73% | 35.16% | 10.79% | 8.32% |
| CN | 56.40% | 29.45% | 4.33% | 9.82% |

BCN and CN were 1.053 and 1.782, respectively, which further proved the existence of N defects in CN.

BET was then used to determine the specific surface area of CN and the pore size distribution of its porous structure. As shown in Fig. 4, the $N_2$ adsorption–desorption isotherms of BCN and CN show IV-type isotherms,[46] and both have a certain degree of an $H_3$-type hysteresis loop, indicating that there are a large number of mesopores in the synthetic material.[20] It can also be seen from the pore size distribution graph that the number of pores of the CN is more than that of BCN, suggesting the higher photocatalytic activity of CN.

Fig. 5a shows the UV-vis absorption spectra of both CN and BCN. The light absorption edge of CN is at 453 nm, and the light response range is wider than that of BCN 443 nm, which is more conducive to light absorption and utilization. The band gap values of BCN and CN were then determined to be 2.70 eV and 2.65 eV, respectively, according to the Tauc plot method (Fig. 5b). It can be seen that the introduction of N defects reduces the $E_g$ of g-$C_3N_4$, makes the light absorption redshift, and broadens the light response range. Due to the weak bonding at the defect site, the splitting between the bonding and the anti-bonding orbitals is reduced, resulting in the formation of electronic states in the band gap, which has a positive effect on the photoexcitation of the electrons, and promotes the narrowing of the band gap, and further expand the range of light absorption.[47–49] During the photodegradation process, the available light absorption of the photocatalyst increases, which is more conducive to the generation of photogenerated electrons, so as to achieve a better photocatalytic effect.

## Photocatalytic activity, recyclability and stability

Fig. S4–S7† present the degradation the first-order degradation kinetics fitting curves of RhB under the photocatalytic reaction with g-$C_3N_4$ that were synthesized by different washing conditions. Based on the data of RhB degradation, the highest RhB degradation efficiency was determined to be the CN that was synthesized by washing with 10 mL 30 °C water and drying at 80 °C for 8 h.

The photocatalytic stability of material CN was then evaluated by RhB photodegradation experiments, and the results are shown in Fig. 6a. It was found that CN maintained a good photocatalytic activity after four cycles degradation of RhB. The recyclability of CN was also confirmed by XRD and SEM data before and after the photocatalytic reactions. As shown in Fig. 6b and c, the crystalline form and morphology (porous lamellar) of CN were not changed after the photocatalytic reactions. In addition, obvious changes of photocatalytic activity of CN in degradation of MO and MB were also not found (Fig. S8†), indicating the high stability and recyclability of CN for organic dyes degradation.

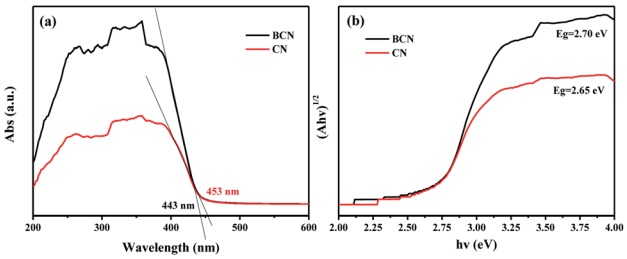


Fig. 5 (a) Ultraviolet diffuse reflectance spectroscopy, (b) energy band spectra of BCN and CN.

## Optical and electrochemical properties

The photoelectrochemical characteristics (photocatalysis mechanism) of CN that involves the photogenerated electron–hole pairs generation post light irradiation was then the photoluminescence (PL) spectra of g-$C_3N_4$ materials were measured and the data were presented in Fig. 7a and S9.† In comparison

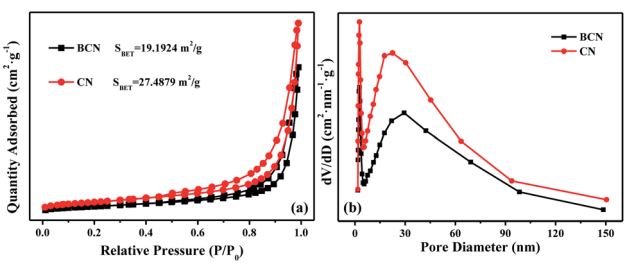


Fig. 4 (a) $N_2$ adsorption–desorption isotherm, (b) aperture distribution curve of BCN and CN.

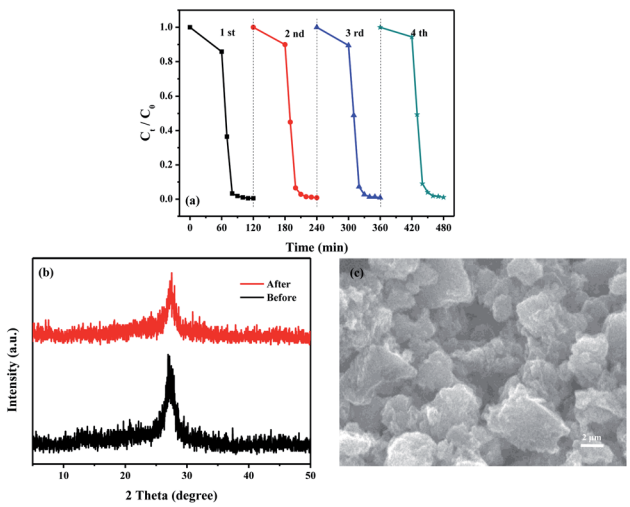


Fig. 6 (a) Cyclic curves for degradation of RhB by CN, (b) XRD patterns and SEM image (c) of CN before and after photodegradation of RhB.

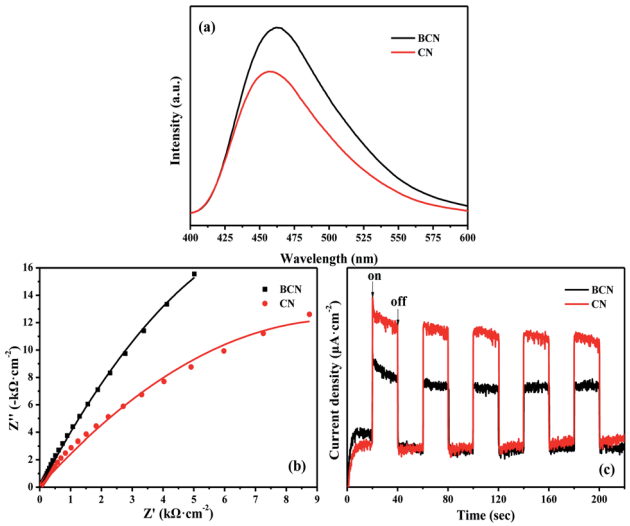


Fig. 7 (a) PL spectra, (b) EIS Nyquist spectrum, and (c) transient photocurrent response of BCN and CN.

with BCN, CN showed lower PL intensity due to its low composite efficiency of photogenerated electrons and holes. As a result of the low composite efficiency, the reaction time of photocatalysis was relatively prolonged and the utilization rate of charge was increased, which contributed to improving the photocatalytic activity.

Next, the separation efficiency of photogenerated electron–hole pairs in CN was examined using a three-electrode system.

Fig. 7b and c show the impedance spectrum (EIS) and transient photocurrent response diagram ($i$–$t$) of BCN and CN. The arc radius of CN in the EIS Nyquist diagram was smaller than that of BCN, indicating its higher photocatalytic activity. As shown in Fig. 7c, without light irradiation, low and stable current densities were observed in both BCN and CN. Upon the light irradiation, the current of both BCN and CN increased rapidly. A much higher photocurrent density was observed for CN in comparison with that of BCN, indicating the higher photocatalytic activity of CN.

### Reactive substances and degradation products analysis

The reactive substances in the CN photocatalytic degradation of RhB reaction system were then investigated. In the photocatalytic reaction containing both CN and RhB, IPA, BQ and EDTA-2Na were added as the trapping agents for $^{\bullet}OH$, $^{\bullet}O_2^-$ and $h^+$, respectively. The $C_t/C_0$ values were then recorded in these three reaction systems. As shown in Fig. 8a, in a photocatalytic reaction system containing CN, RhB and BQ, the degradation of RhB is significantly inhibited. In sharp contrast, obvious decreases of RhB degradation were not observed for the reactions containing IPA and EDTA-2Na. This inhibition experiment implies that $^{\bullet}O_2^-$ is the main active substance for photocatalysis reaction.

The CN-mediated RhB degradation system products were then detected by high-performance liquid chromatography (HPLC). As shown in Fig. 8b, RhB showed a retention time of

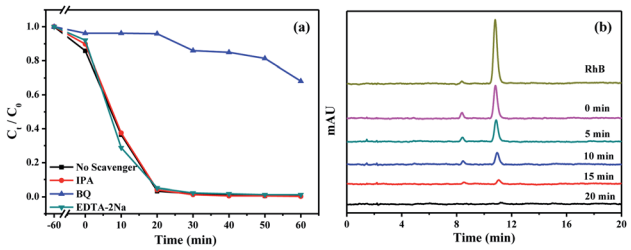


Fig. 8 (a) Trapping experiment of RhB free radical degradation by CN, and (b) HPLC determination of RhB products degraded by CN.

11.495 min. Upon light irradiation, the HPLC peak at 11.495 min was gradually decreased and finally disappeared after 20 min light irradiation, suggesting the completion degradation within 20 min light irradiation.

## Conclusion

In summary, a nitrogen-deficient porous g-$C_3N_4$ photocatalyst was prepared and characterized as a photocatalyst for photocatalytic degradation of RhB. After modification under the optimal washing conditions, the nitrogen-deficient porous g-$C_3N_4$ photocatalyst can effectively degrade RhB dyes under simulated visible light. The study found that the degradation reaction can be completed within 20 minutes of light irradiation, which was confirmed by UV-vis absorption and HPLC results. This new type of photocatalyst has high photocatalytic activity, recyclability and stability, making it useful for degradation of RhB and other organic dyes such as MO and MB under visible light irradiation. It is anticipated that this photocatalyst to be used for future wastewater treatment.

## Conflicts of interest

There are no conflicts to declare.

## Acknowledgements

This work was financially supported by the National Natural Science Foundation of China (21777130, 41807210), the Natural Science Foundation of Sichuan Province of China (2019YJ0522, 2018JY0184), the Meritocracy Research Funds of China West Normal University (463132) and the Fundamental Research Funds of China West Normal University (416390). R. Zhang acknowledged the National Health and Medical Research Council (APP1175808).

## Notes and references

1 P. Wang, L. Yang, J. Li and B. Sadeh, *Catal. Lett.*, 2020, **150**, 1985–1992.
2 L. Qiu, Z. Zhou, M. Ma, P. Li, J. Lu, Y. Hou, X. Chen and S. Duo, *Materials*, 2019, **12**, 3948.
3 L. Qu, G. Zhu, J. Ji, T. P. Yadav, Y. Chen, G. Yang, H. Xu and H. Li, *ACS Appl. Mater. Interfaces*, 2018, **10**, 42427–42435.

4 L. Bai, S. Wang, Z. Wang, E. Hong, Y. Wang, C. Xia and B. Wang, *Environ. Pollut.*, 2019, **248**, 516–525.
5 S. Guan, R. Li, X. Sun, T. Xian and H. Yang, *Mater. Technol.*, 2020, **35**, 1782062–1782074.
6 A. A. Yaqoob, N. H. b. M. Noor, K. Umar, R. Adnan, M. N. M. Ibrahim and M. Rashid, *Appl. Nanosci.*, 2021, **11**, 1291–1302.
7 Y. Zhang, A. Sun, M. Xiong, D. K. Macharia, J. Liu, Z. Chen, M. Li and L. Zhang, *Chem. Eng. J.*, 2021, **415**, 129019.
8 P. Basnet, D. Samanta, T. I. Chanu and S. Chatterjee, *J. Alloys Compd.*, 2021, **867**, 158870.
9 M. Y. Rather and S. Sundarapandian, *J. Cluster Sci.*, 2021, **34**, 349545191–349545201.
10 C. Lv, L. Wang, X. Liu, L. Zhao, X. Lan and J. Shi, *Appl. Surf. Sci.*, 2020, **527**, 146726.
11 Q. Zhang, H. Zhao, Y. Dong, X. Zhu, X. Liu and H. Li, *New J. Chem.*, 2021, **45**, 1327–1338.
12 M. J. Fakharian-Qomi and A. Sadeghzadeh-Attar, *ChemistrySelect*, 2020, **5**, 6001–6010.
13 N. Yavari, O. Tavakoli and M. J. Parnian, *Chem. Pap.*, 2021, **75**, 3181–3196.
14 Y. Zhang, G. Zhao, Y. Xuan, L. Gan and M. Pan, *Cellulose*, 2021, **28**, 991–1009.
15 A. Wang, C. Wang, L. Fu, W. Wong-Ng and Y. Lan, *Nano-Micro Lett.*, 2017, **9**, 47.
16 C. Prasad, H. Tang and I. Bahadur, *J. Mol. Liq.*, 2019, **281**, 634–654.
17 C. Xiong, Q. Ren, X. Liu, Z. Jin, Y. Ding, H. Zhu, J. Li and R. Chen, *Appl. Surf. Sci.*, 2021, **543**, 148844.
18 Q. Sun, X. Hu, S. Zheng, J. Zhang and J. Sheng, *Environ. Pollut.*, 2019, **245**, 53–62.
19 Z. Cai, Z. Song and L. Guo, *ACS Appl. Mater. Interfaces*, 2019, **11**, 12770–12776.
20 Y. Li, S. Wang, W. Chang, L. Zhang, Z. Wu, R. Jin and Y. Xing, *Appl. Catal., B*, 2020, **274**, 119116.
21 C. Sun, J. Dai, H. Zhang, S. Li and A. Wang, *J. Mater. Sci.*, 2021, **56**, 7557–7572.
22 X. Bai, X. Wang, X. Lu, S. Hou, B. Sun, C. Wang, T. Jia and S. Yang, *CrystEngComm*, 2021, **23**, 1366–1376.
23 J. Gong, Z. Xie, C. Xiong, C. Liu, Z. Li and Z. Le, *J. Radioanal. Nucl. Chem.*, 2019, **322**, 1115–1125.
24 J. Xue, S. Ma, Y. Zhou, Z. Zhang and M. He, *ACS Appl. Mater. Interfaces*, 2015, **7**, 9630–9637.
25 J. E. Ellis, D. C. Sorescu, S. I. Hwang, S. C. Burkert, D. L. White, H. Kim and A. Star, *ACS Appl. Mater. Interfaces*, 2019, **11**, 41588–41594.
26 C. Jin, W. Li, Y. Chen, R. Li, J. Huo, Q. He and Y. Wang, *Ind. Eng. Chem. Res.*, 2020, **59**, 2860–2873.
27 K. Koci, M. Reli, I. Troppova, M. Sihor, T. Bajcarova, M. Ritz, J. Pavlovsky and P. Praus, *Catalysts*, 2019, **9**, 735.
28 M. Nemiwal, T. C. Zhang and D. Kumar, *Sci. Total Environ.*, 2021, **767**, 144896.
29 S. Patnaik, D. P. Sahoo and K. Parida, *Carbon*, 2021, **172**, 682–711.
30 J. Yi, W. El-Alami, Y. Song, H. Li, P. M. Ajayan and H. Xu, *Chem. Eng. J.*, 2020, **382**, 122812.
31 A. Kundu, S. Sharma and S. Basu, *J. Phys. Chem. Solids*, 2021, **154**, 110064.
32 J. Di, Y. Lu, W. Wang, X. Wang, C. Yu, J. Zhao, F. Zhang and S. Gao, *J. Phys. Chem. Solids*, 2021, **155**, 110114–110122.
33 Y. Du, L. Zhao, H. Chen, Z. Huang, X. He, W. Fang, W. Li, X. Zeng and F. Zhang, *J. Mater. Sci.*, 2019, **55**, 1973–1983.
34 H. Kim, S. Gim, T. H. Jeon, H. Kim and W. Choi, *ACS Appl. Mater. Interfaces*, 2017, **9**, 40360–40368.
35 Z. Liu, H. Zheng, H. Yang, L. Hao, L. Wen, T. Xu and S. Wu, *RSC Adv.*, 2016, **6**, 54215–54225.
36 F. Zhao, K. K. Khaing, D. Yin, B. Liu, T. Chen, C. Wu, K. Huang, L. Deng and L. Li, *RSC Adv.*, 2018, **8**, 42308–42321.
37 Q. Liang, X. Liu, J. Wang, Y. Liu, Z. Liu, L. Tang, B. Shao, W. Zhang, S. Gong, M. Cheng, Q. He and C. Feng, *J. Hazard. Mater.*, 2021, **401**, 123355.
38 C. T. Seto, J. P. Mathias and G. M. Whitesides, *J. Am. Chem. Soc.*, 1993, **115**, 1321–1329.
39 S. Zhao, Y. Zhang, J. Fang, H. Zhang, Y. Wang, Y. Zhou, W. Chen and C. Zhang, *ACS Sustainable Chem. Eng.*, 2018, **6**, 8291–8299.
40 S. Seyyed Shahabi, N. Azizi, V. Vatanpour and N. Yousefimehr, *Sep. Purif. Technol.*, 2020, **235**, 116134.
41 J. Wu, X. Ji, X. Yuan, Z. Zhao, Y. Li, B. Wen, H. Zhang, D. Yu, Y. Zhao and Y. Tian, *Chem. Mater.*, 2019, **31**, 9188–9199.
42 X. Liang, G. Wang, X. Dong, G. Wang, H. Ma and X. Zhang, *ACS Appl. Nano Mater.*, 2019, **2**, 517–524.
43 J. Xu, Z. Wang and Y. Zhu, *ACS Appl. Mater. Interfaces*, 2017, **9**, 27727–27735.
44 L. Liang, Y. Cong, F. Wang, L. Yao and L. Shi, *Mater. Res. Express*, 2019, **6**, 086207.
45 H. Tang, R. Wang, C. Zhao, Z. Chen, X. Yang, D. Bukhvalov, Z. Lin and Q. Liu, *Chem. Eng. J.*, 2019, **374**, 1064–1075.
46 J.-H. Zhang, M.-J. Wei, Z.-W. Wei, M. Pan and C.-Y. Su, *ACS Appl. Nano Mater.*, 2020, **3**, 1010–1018.
47 S. Bai, N. Zhang, C. Gao and Y. Xiong, *Nano Energy*, 2018, **53**, 296–336.
48 R. Qi, P. Yu, J. Zhang, W. Guo, Y. He, H. Hojo, H. Einaga, Q. Zhang, X. Liu, Z. Jiang and W. Shangguan, *Appl. Catal., B*, 2020, **274**, 119099–119110.
49 J. Wang, B. Gao, M. Dou, X. Huang and Z. Ma, *Environ. Res.*, 2020, **184**, 109339–109348.